Published in final edited form as:
Magn Reson Med. 2012 June ; 67(6): 1600–1608. doi:10.1002/mrm.23144.

Improved Least Squares MR Image Reconstruction Using Estimates of k-Space Data Consistency

Kevin M. Johnson, Ph.D.[1], **Walter F. Block, Ph.D.**[1,2,3], **Scott. B. Reeder, Ph.D., M.D.**[1,2,3,4], and **Alexey Samsonov, Ph.D.**[1,2]

[1]Department of Medical Physics, University of Wisconsin, Madison, WI

[2]Department of Radiology, University of Wisconsin, Madison, WI

[3]Department of Biomedical Engineering, University of Wisconsin, Madison, WI

[4]Department of Medicine, University of Wisconsin, Madison, WI

Abstract

This work describes a new approach to reconstruct data that has been corrupted by unfavorable magnetization evolution. In this new framework, images are reconstructed in a weighted least squares fashion using all available data and a measure of consistency determined from the data itself. The reconstruction scheme optimally balances uncertainties from noise error with those from data inconsistency, is compatible with methods that model signal corruption, and may be advantageous for more accurate and precise reconstruction with many least-squares based image estimation techniques including parallel imaging and constrained reconstruction/compressed sensing applications. Performance of the several variants of the algorithm tailored for fast spin echo (FSE) and self gated respiratory gating applications was evaluated in simulations, phantom experiments, and in-vivo scans. The data consistency weighting technique substantially improved image quality and reduced noise as compared to traditional reconstruction approaches.

Introduction

MR data may be corrupted either within a single encoding readout (intra-readout) or between subsequent readouts (inter-readout). Within a readout window, signal is subject to magnetization evolution caused by rapid effects such as flow, off-resonance, and T2/T2* decay. Between different readout acquisitions, slower effects such as non-steady state conditions, physiologic variations, and/or contrast uptake may lead to inconsistent signals between readouts. Intra- and inter-readout inconsistencies cause the majority of artifacts in MR images and in many situations they can severely degrade image quality.

Parallel imaging (1,2) and constrained reconstruction techniques (e.g. compressed sensing (3,4), homodyne (5), etc) have been very successful in reducing the number of readouts required to reconstruct images. These techniques allow shorter data collection periods without dramatic modifications to the acquisition resulting in more consistent data for images at a given resolution. As an example, shortening the acquisition time using parallel imaging results in images with both less blurring and better vessel conspicuity in contrast enhanced venography using conventional extracellular gadolinium based contrast agents (6). However, even with parallel imaging and advanced reconstruction techniques, many applications still require imaging times much longer than potential signal variations. For

Corresponding Author and Reprint Info: Kevin Johnson, University of Wisconsin – Madison, 1122l Wisconsin Institutes Medical Research, 1111 Highland Ave., Department of MR/CT Research, Madison, WI53705-2275, Phone (608) 265-9688, kmjohnson3@wisc.edu.

these reasons, robust imaging requires a balance between the desired imaging parameters and artifacts from rapid signal variations (flow, off-resonance, etc) and those from slow signal variations (contrast washout, heart rate variations, etc).

To shorten the overall image acquisition time (i.e. temporal footprint), many sequences have been modified to collect more data within a given repetition time (TR) using multi-echo and non-Cartesian sampling. Multiple spin-echo sequences (7) (FSE/RARE) have all but replaced inefficient, single echo sequences. Furthermore, recently developed variable flip angle refocusing allow longer echo trains, resulting in more than a hundred fold increase in acquisition efficiency over single echo sequences, facilitating clinical use of 3D FSE imaging (8,9). Gradient echo data can be also collected more efficiently by utilizing alternative k-space sampling patterns such as echo-planar imaging (EPI), spiral and radial trajectories. These trajectories have enabled acquisition of time consuming and/or time sensitive acquisitions such as diffusion weighted and functional imaging. Multi-echo gradient and spin-echo techniques, as well as hybrid approaches such as GRASE (10), shorten acquisition times allowing reduced effects from slow variations, such as respiratory motion. However, these techniques introduce greater sensitivity to data inconsistencies arising from rapid magnetization relaxation, eddy currents, motion, off-resonance, diffusion, and spin refocusing. With additional information or constraints, artifacts caused by data inconsistencies can be greatly reduced (i.e. off-resonance(11,12)). However, many inconsistencies cannot be corrected, which results in artifacts that worsen as the length of the readout or the number of echoes increases.

Using parallel imaging in combination with shorter readouts results in images with reduced sensitivity to data inconsistencies compared to efficient readouts alone. For example, in single shot EPI utilizing a shorter echo train and relying on parallel imaging to fill missing lines results in images with reduced distortion (13). Robust imaging requires the echo train length and parallel imaging acceleration factor be chosen to balance artifacts from data inconsistency with artifacts from g-factor noise amplification. In such serial combinations, lines in k-space are either generated by synthesis with parallel imaging or by direct sampling and there is no simple method to generate a line using the potentially noisy estimate from PI in combination with the potentially inconsistent information from EPI. As an example, even after phase correction algorithms are applied EPI ghosting artifacts are often present due to inconsistencies between even and odd echoes. The odd lines in k-space could be discarded and parallel imaging could be utilized to unwrap images(14); however, current methods do not support the mutual generation of odd lines using the sampled data and parallel imaging.

Over the past decade, least squares estimation has become increasingly popular in many modern reconstruction approaches for MRI data. Virtually all parallel imaging based techniques utilize least squares estimation alone or in combination with more traditional approaches such as gridding for direct estimation of images (e.g. sensitivity encoding (SENSE(2,15))) and/or for the estimating of missing data (e.g. generalized auto calibrating partially parallel acquisitions (GRAPPA_(16))). Furthermore, developing frameworks for constrained reconstruction/compressed sensing techniques also rely heavily on similar optimization-based image estimation. The optimization-based methods introduce greater flexibility in handling data with unequal quality. In this work, we develop a technique for harnessing regular least squares based reconstruction techniques in situations where data is not consistent. The proposed approach utilizes estimated inconsistencies with an optimized reconstruction to balance artifacts from acceleration with those associated with the use of inconsistent data. Our technique is evaluated using radial trajectories for both fast spin echo imaging and respiratory-gated acquisitions.

Theory

Standard reconstruction approaches aim to find an optimal inverse to the forward signal model:

$$s=Ex+\varepsilon \quad \text{Eq 1}$$

where E is the sampling operator (when discretized, E is the encoding matrix), x is the image, ε is noise error, and s is the raw collected data. The sampling operator traditionally includes Fourier transform (and coil sensitivity (2) terms in case of parallel imaging reconstruction). If more complete description is required, the sampling operator may be modified to model additional physical processes (for example, off-resonance effects (17), and the prior knowledge of T2/T2* decay in image space (18)). However, a limited set of physical phenomena is often modeled in E, as the consideration of all imaging imperfections is infeasible from theoretical and/or computational perspectives. If noise error is independent and identical distributed Gaussian, the discrete, SNR-optimized approach to estimate the image is achieved by minimizing the squared difference between the collected data and that simulated from the image:

$$x=\arg\min_x \| D^{1/2}(Ex-s) \|_2^2 \quad \text{Eq 2}$$

where D is a weighting matrix. For optimal noise performance with perfect data (i.e. when encoding matrix is accurate and models the physics of the signal accurately), D should be equal to the inverse of the noise covariance matrix (15). For variable density sequences, an alternative choice of D is the inverse of local sampling density, in which SNR optimality is traded in favor of improved convergence of iterative solutions of Eq. [2]. In the following description, we will consider only situations targeted at optimized performance of the estimation without consideration of convergence issues. We assume that the noise covariance matrix and its inverse (D) is the identity, which may be reached by proper noise pre-whitening (15).

The least squares solution in Eq. 2 assumes that E perfectly describes data collection without any systematic bias and x is identical for all samples. Since the magnetization changes over time, both E and x are time dependent. In order to account for any systematic bias and/or the model mismatch, we consider the forward model of Eq. 1 extended with an additional term to account for these errors:

$$s=Ex+\varepsilon+f \quad \text{Eq 3}$$

where f is systematic measurement error. Unlike noise error (ε), f is non-stochastic error. Least squares solutions to Eq. 3 ignore f and assume the error to have a known distribution (i.e. white, zero mean Gaussian). These solutions will have artifacts and sub optimal noise performance. With full knowledge of the distribution of f for every point, a maximum likelihood estimate for x could be derived; however, the distribution is generally not known and due to time constraints such reconstructions would not be practical in-vivo. To improve the estimation of x without detailed knowledge of the distribution of f, a reasonable solution is to introduce into the least squares solution an uncertainty weighting matrix in addition to the noise covariance matrix (Eq. 2), both of which are derived from bounds on the uncertainty defined in deterministic and probabilistic ways, respectively. This uncertainty weighting matrix may be estimated, for example, as follows (19):

$$G=diag(1/|f|) \quad \text{Eq 4}$$

The resulting least squares estimation may be expressed as follows:

$$\widehat{x}=\arg\min_x \| G^{1/2} D^{1/2} (Ex - s) \|_2^2 \quad \text{Eq 5}$$

Intuitively, samples with a high level of systematic bias will be weighted lower than those with low levels of bias, and the solution will trend towards the unbiased solution. This treatment of data uncertainty is similar to the treatment of noise uncertainty from sources of unequal variance. Subsequently, the performance of this method will be optimal when the distribution of errors are zero mean and uncorrelated. This formulation requires knowledge of $|f|$ at every point in k-space which is not generally known and can be difficult/infeasible to estimate. Below, we consider several possible scenarios for approximate construction of the uncertainty weighting matrix G.

Data Uncertainty Estimation

Many sources of data corruption are also sources of desired contrast. For example, T2 decay along FSE echo trains creates desired image contrast at the effective echo time but also causes blurring due to signal variation over the rest of the echo train. To drive an iterative reconstruction towards the desired contrast at the effective echo time, one can consider the signal at the effective echo time to be ideal. At this chosen point in time, the encoding is described exactly by Eq. 1 and all errors are caused by noise. The systematic error f may be estimated in respect to the reference contrast point subtracting two samples at the same point in k-space but at different times:

$$s(t) - s_{ref} = f + \varepsilon \quad \text{Eq 6}$$

where $s(t)$ is the signal, s_{ref} is the signal at the reference point, and ε is the error term due to stochastic noise. The magnitude of the signal strongly decreases with increasing distance from the center of k-space and the systematic error, f, is also expected to decrease. Subsequently, the stochastic error term in equation Eq. 6 will be dominant at the edge of k-space. To reduce the effects of stochastic error and minimize the time required, we propose to estimate f at a repeatedly sampled k-space center using Eq. 6, and approximate it using signal modeling elsewhere. Repeated samples can come from FID sampling (20), calibration pre-scans, or Non-Cartesian sampling trajectories such as radial or spirals. Once the f is approximated, the weighting matrix can be determined:

$$G = \frac{1}{\sigma + |f|} \quad \text{Eq 7}$$

where σ is a small value to avoid division by zero, which may be chosen for example to be on the order of noise level. Several specific signal modeling approaches to find f are detailed in the next section.

Methods

All experiments were performed on or assumed the performance of a clinical 3.0T scanner (MR750, GE Healthcare, Waukesha, WI; slew rate: 200 T/m/s, max gradient strength: 50 mT/m). Each sequence utilized a 4-half line radial k-space trajectory (21) which collects 4-half radial projections starting and ending at the center of k-space.

Application to Fast Spin Echo (FSE) Imaging

Deriving Data Inconsistency—In FSE, data inconsistency sources can be split into inter-readout and intra-readout errors. Inter-readout signal variations signal variations occur due to different refocusing flip angles, refocusing of spins, and signal relaxation. Intra-

readout errors are caused by free precession of the signal between RF pulses and for are generally well described by off-resonance and T2* decay about a central refocusing time. The effective T2* decay and off-resonance effects change from readout to readout due to unequal T1/T2 relaxation of signal constituents; however, we expect the change in T2* and off-resonance to be relatively small over the echo train. In this work, we assume these two effects are separable. For standard FSE acquisitions, intra-readout errors are often considered negligible but cannot be neglected for rapid acquisitions with longer readout windows such as FSE with multiple echo (GRASE) and spiral trajectories. We utilized a highly efficient 4-half line radial trajectory, which is similar to radial GRASE (22) but has a shorter readout duration than previous applications. In the absence of trajectory errors, this trajectory samples the center of k-space every readout, inter-readout signal uncertainty can be estimated entirely from the center of k-space using Eq. 6. To estimate uncertainty along the intra-readout direction, modeling must be performed. In this work, we model the intra-readout signal using average T2* decay and an off-resonance spectrum:

$$S(t)=e^{-\frac{|t|}{T2*}}\int\rho(\omega)e^{i\omega t}\,d\omega \qquad \text{Eq 8}$$

where t is the time from the center of the readout, ω is the normalized off-resonance frequency, $\rho(\omega)$ is an estimated or measured off-resonance spectrum. The measurement error can then be estimated as follows:

$$G(i,t)=\frac{1}{\sigma+\left|s_i S(t)-s_{ref}\,S(0)\right|} \qquad \text{Eq 9}$$

where i is the position in the echo train, s_i is the signal from the center of k-space at echo i. For all FSE experiments presented, the reference signal was set to the central (i =64) echo of the first shot. The off-resonance spectrum was estimated using separate Gaussian distributions for fat and water, both with full width half max of 100 Hz. The ratio of water to fat was modeled at 2 to 1 and the average T2* was set to 50ms.

Simulations—Realistic 2D single-shot Fast Spin Echo (FSE) data were simulated using a single slice from the BrainWeb fuzzy anatomical model for a normal subject (23). Within the echo train, radial lines are distributed with a pseudorandom ordering (24). This ordering scheme creates local data inconsistencies in k-space resulting in reduced coherent artifacts compared to sequential ordering(25). Coil sensitivities were measured in phantom with an 8-channel brain coil and utilized for both simulated acquisition and reconstruction (HD Brain Array, GE Healthcare, Waukesha, WI). B0 field heterogeneity was simulated with a two dimensional Gaussian function, centered above the sinuses with a maximum offset of 400 Hz and symmetric full width half max of 5.5 cm. Acquisition was simulated at 1×1×4 mm^3 resolution by inverse gridding the discrete Fourier transform of the multiplication of off-resonance, sensitivity, and signal images for each sample. Signal images were derived utilizing Bloch equations for each echo using a variable flip angle FSE acquisition with TR= 2200ms, echo spacing of 4.5ms, and an echo train length (ETL) of 128. Iterative Conjugate gradient (CG) SENSE image reconstructions were performed with uniform weights (G = *Identity*) and proposed weights using 100 repeated measurements with different complex noise realizations. The CG algorithm was reinitialized every 10 iterations to reduce numerical truncation errors and stopped once the residual was 10^6 times lower than the initial guess of zeroes or 100 iterations had been performed. The noise level was set corresponding to an SNR of 300 with respect to maximum k-space value (at the center of k-space). Parameter σ in Eq. 8 was set to the same value. Inter-readout signal modulation (decay along the echo train) was estimated from the center of k-space for each readout. Reconstructed images were separated into mean (accuracy) and noise (precision)

components assuming zero mean Gaussian noise. The average noise level over the extent of the phantom was measured. Normalized Root Mean Square Error (RMSE) was computed for the mean signal with reference to ideal images. Ideal images were considered the average signal over all 128 echoes for uniform weighting and the image at the 64th echo for weighted reconstruction. This is to compensate for the shorter and heterogeneous effective TE when uniform weighting is utilized. To compute the effective resolution, we computed the local point spread function (PSF) utilizing a variation of a local perturbation technique (26):

$$PSF_i = \frac{\widehat{x}[S(x * (I + a\delta_i))] - \widehat{x}[S(x)]}{a} \quad \text{Eq 10}$$

where $\hat{x}$ is the estimated image with and without weighting, I is the identity matrix, δ_i is the delta function at the ith pixel, S is the exact signal modeling, and a is the magnitude of the perturbation. The spatially dependent PSF was computed with and without weighting using a =0.05. Due to very long computational times for the PSF computation, the PSF was only computed for every fourth pixel in both matrix dimensions. For each PSF, the full width half max (FWHM) was computed as compared to the expected resolution.

In-Vivo 3D Radial Fast Spin Echo—Additionally, we implemented a 3D radial, variable flip angle, fast spin echo (FSE) pulse sequence. In-vivo 3D radial FSE images were acquired with parameters similar to simulation studies (TR=2200ms, Resolution = 1mm^3, ETL=128, echo spacing=4.5ms, 4-half line radial trajectory). Imaging was performed with a multi-shot 3D acquisition requiring 55 shots of 128 echoes utilizing a 32 channel head coil (MR Instruments, Minneapolis, MN, USA). Projection ordering was interleaved with a 2D extension of the bit-reverse algorithm (24) described in the appendix. Sensitivity maps were estimated from the full sampled central k-space data (27). Parameter σ was determined utilizing the standard deviation of the k-space central point of all 64th echoes. Images were reconstructed without weighting and with inter-readout and/or intra-readout weighting.

Application to Retrospective Respiratory Gating

Current methods for respiratory motion gating acquire data during an acquisition window. During this window, some motion is present, but is considered negligible by most reconstructions. For techniques that frequently update respiratory motion measures, such as self gating (28) or bellows, data consistency weighting can be utilized as an alternative method to perform gating. To test this, images were acquired with a free breathing 4-half line, 3D radial spoiled gradient echo (SPGR) acquisition utilizing a 32 channel torso array coil (NeoCoil, Pewaukee, WI, USA). During acquisition a respiratory bellows data was recorded but no gating was performed. Projections were acquired with the 2D bit reverse algorithm, with N equal number of TR's per heart beat and M equal to the total number of projections divided by N (See Appendix). This interleaving allows retrospective choice of data with minimal artifacts from uneven projection spacing and reduces the prevalence of artifacts from cardiac pulsatility. The heart rate was fixed to be 60 bpm and was not changed per subject. The total number of projections acquired was 29,998 for a total scan time of 2:40 min. Other relevant parameters include: TR=4.2ms, resolution=1.25×1.25×1.25mm^3, flip angle = 12°, FOV = 32×32×24cm^3. We first applied this protocol to acquire images of resolution phantom in the presence of table motion simulating respiratory motion. A sinusoidal motion pattern was utilized with a cycle of 3s and maximum displacement of 7mm. Respiratory bellows information was placed in a 200 bin histogram. The median value of the center of k-space for projections within the most common end-expiration bin was set as the signal reference. The signal difference was then computed for all projections utilizing Eq. 6. Images were then reconstructed utilizing: 1) all projection with signal difference less

than 50% of the maximum, 2) all projection with signal difference less than 20% of the maximum, and 3) weighting determined with Eq. 7 assuming an SNR of 300. To avoid errors from trajectory errors, the center of k-space was evaluated at the first echo which is effectively FID. No intra-readout weighting was utilized. Image artifact levels were measured utilizing a manual drawn ROI within the air spaces of the phantom. Subsequent images were acquired with the identical protocol and reconstruction schemes in a volunteer and qualitatively analyzed for image quality.

Results

FSE

Figure 1 shows representative images reconstructed from the digital phantom, the computed mean error, the noise, and the FWHM. Images utilizing uniform weighting average the center of k-space amongst all echoes. This effectively reduces T2 contrast and precludes the use of an effective echo time to describe the images. Images with the inconsistency weighting can be described by a single effective echo time, which can be determined from the chosen reference image. Residual images utilize matched truth images and subsequently do not reflect this bulk change in contrast. Without the bulk change in contrast, weighted images still show a substantial reduction in RMSE from 9.6% in uniform weighted image to 2.3% in weighted images. The largest errors are seen in the anterior sections of the brain, where off-resonance from the nasal cavities was simulated. Unlike the mean error, noise is evenly distributed across the images in both acquisitions and lower in images with inconsistency weighting. The average noise level is reduced from 1.6% in uniformly weighted images to 1.1% in images with the proposed weighting. Both the proposed weighting and uniform weights produced high resolution images with average FWHM of 0.9941 and 1.0074 respectively. Convergence was slower for weighted images with a median of 48 iterations vs. 31 iterations for uniform weighting.

In-vivo signal at the center of k-space, derived weighting functions, and k-space radius are shown in Figure 2. From the center of k-space along echo train, we can clearly see rapid signal decay during the initial period of signal stabilization followed by a period of relatively flat signal until constant signal cannot be obtained and the signal decays rapidly again. The derived weighting function (Figure 2b) along the echo train reflects these changes in signal, with the periods of stabilization and final decay weighted lower than during the period of relatively constant signal. The weighting function derived along the readout direction (Figure 2d) is symmetric with a near exponential decay. Comparing this to the k-space trajectory shown in Figure 2c, we can see a 100-fold reduction in weighting for the longer echoes. Applying these weights, reconstructed images are shown in Figure 3. Similar to numerical simulations, substantial signal dropout is observed in the nasal cavities for uniform weighting which is not present in the weighted reconstructions using weighting in the readout directions (Figures 3b/3c). Similar imaging utilizing weighting along the echo train dimension (Figures 3b/3d) have better gray/white matter contrast. Images reconstructed with weighting along both the readout and echo train dimension represents a compromise between artifacts in both dimensions but has the highest image quality.

Respiratory Gating

Figure 4 shows reconstructed images from phantom motion experiments. Acquisition efficiency was 19% and 47% for 10% and 50% thresholds. Significant motion blur is observed in 50% threshold images as well as additional background artifact. 10% threshold images have minimal observed motion blur, but show artifacts from undersampling. Weighted phantom images represent the best of both worlds, with no observable motion blur and minimal artifact. The mean artifact level was lowest in weighted images at 6.2%. The

10% and 50% images had high mean artifact levels with values of 11.4% and 6.4%, respectively. Figure 5 shows in-vivo signal difference waveforms, threshold levels, and the corresponding weighting functions for the first 8 seconds. The acquisition efficiency for thresholded images was 72.4% and 23.5% for the 50% and 10% thresholded images, respectively. Figure 6 shows corresponding coronal and sagittal reformats of the in-vivo images. Images with 50% thresholding show substantial blurring, obscuring the visualization of structures within the liver. Images from a threshold of 10% do not exhibit significant motion blur; however, artifacts from undersampling similarly obscure small structures. Images reconstructed with weighting do not have significant blur and do not have substantial artifacts from undersampling.

Discussion

We have presented a method for weighted least squares reconstruction of inconsistent MRI data samples. The method aims to achieve optimized reconstruction from inconsistent data by including information about the expected level of systematic errors in the data to weight samples in a least squares reconstruction. We utilized several different ways to estimate k-space data consistency such as estimation of consistency from the data itself using resampled data points, from FID navigators (20), or from modeling the expected signal corruption. We have demonstrated substantial improvements in image quality for multiple echo acquisition techniques and for respiratory gating applications. The formalism developed in the paper (Eqs. 3-7) may be applicable to other applications utilizing arbitrary sampling patterns that creates local inconsistencies in k-space and allows inferring the inconsistencies using the aforementioned and/or other possible approaches. Since least squares reconstruction is utilized in almost all parallel imaging reconstruction schemes, minimal modification is required to incorporate advanced reconstruction techniques such as compressed sensing (3).

Weighted least squares reconstructions are an evolution of discrete weighting schemes such as strict thresholding (29), keyhole angiography (30), tornado filtering (31) and KWIC T2 weighting (24). Discrete methods preferentially weight data taken at the desired time point or image contrast, but ultimately must use inconsistent data over a wider interval to fill remaining gaps in k-space. Moreover, many of those methods were designed for gridding reconstruction, and straightforward extension of those approaches to iterative estimation may be suboptimal. With parallel imaging, compressed sensing, or sampling redundancies, it is often unclear whether more undersampling/less averaging will produce better images than utilizing data that is inconsistent. The weighted approach first determines how consistent the data are, and then determines how much data should be utilized. This approach allows reconstructing of images with complex k-space pattern or multiple sources of signal corruptions where it is often difficult to design discrete weighting schemes. Both the previously described discrete and our continuous weighting schemes help address contrast difference between non-Cartesian and Cartesian acquisitions. Since non-Cartesian acquisitions often resample points in k-space without weighting, the final image is an average of all points. As shown in our fast spin echo experiment such averaging can lead to decreased contrast in the final image and difficultly in assigning a single echo time.

The proposed weighted least squares approach is related to an iteratively reweighted least squares estimation used in implementation of Lp norms (p>=1) minimization or in robust regression (32). For example, from reweighted least squares estimation, we know that the Lp norm of the residual is equivalent to an iteratively reweighted L2 norm:

$$x_{n+1}=\arg\min_x \| W_n^{1/2}(Ex - s) \|_2^2 \qquad \text{Eq 11}$$

where W is a reweighting matrix that is iteratively updated. For L1 minimization, W is the inverse of the error term:

$$W_n = diag(Ex_n - s)^{-1} \quad \text{Eq 12}$$

If x_n is the ideal image and noise is ignored this L1 weighting will be identical to that utilized in Eq 7. However, x_n will only converge to the ideal image if inconsistent data are considered as outliers in otherwise normal distribution (33). This makes L1 minimization more effective than L2 minimization in low noise situations in cases of incidentally motion or other situations in which only a few samples are corrupt (34). However, estimation with L1 norms will not be effective in cases where there are a large number of inconsistent samples/outliers or there is no heuristic to make decision on which values are outliers (for example, in case of slow steady increase in errors). Additionally, using prior weighting dramatically reduces computation time and may improve noise performance. In our simulations, we observed a decrease in noise in images when weighting was used. One possible explanation is that the proposed weighting helps distinguish between noise error and inconsistency error leading to a better noise performance in least squares estimation that assumes normally distributed noise.

The proposed weighted reconstruction is expected to be most effective where data inconsistencies are localized in k-space. This is due to the fact that most least squares estimation approaches employed in parallel MRI and constrained iterative reconstruction are generally only capable of filling local gaps of data in k-space. For the pseudo randomly ordered radial acquisition utilized, data in each region of k-space comes from a variety of sampling times and can be very inconsistent. In some cases, the appearance of artifacts from acquisition ordering schemes with smooth signal variations may be preferred over those that create local data inconsistencies. For example, 3D Cartesian fast spin echo trains are often acquired with sequential encoding of echoes (35). This creates a global inconsistency confined to a single direction, and leads to T2 blurring. The weighted reconstruction would not resolve this blurring. However, if the data were acquired in an interleaved or random ordering, weighting may improve the reconstruction, although may produce artifacts with less favorable appearance such as ghosting artifacts. Parallel imaging, compressed sensing/constrained reconstruction performance may be favorable to minimize those artifacts. The comparison of the developed 3D FSE pulse sequence with its Cartesian counterpart is subject of future work.

Further investigation is warranted to apply the weighting approach to constrained reconstruction other parallel imaging approaches, imaging trajectories and applications. The parallel imaging formulation we have presented utilizes SENSE which has some disadvantages compared to auto-calibrated k-space based reconstructions, like GRAPPA (16). Implementation of the proposed weighting least squares reconstruction for k-space approaches is an open problem. Kernels would need to be computed for each point using the weights of data consistency, which may be impossible given a limited calibration region. This could be resolved by utilizing an image domain based GRAPPA approach like the recently proposed SPIRIT reconstruction (36). This has the additional advantage of being easily combined with Non-Cartesian and Compressed Sensing approaches but has notably higher computation than standard GRAPPA and traditional iterative SENSE reconstructions. In this work, we have only investigated a single trajectory in two applications. In other MRI imaging techniques with significant data inconsistencies, similar improvements can be expected; however, it may be more difficult to determine consistency weights. For example, we have utilized repeated sampling of the center of k-space to determine weighting. For some Cartesian applications the center of k-space can be acquired before pre-winding gradients with minimal penalty (20) while for others this can be more challenging (for

example, for fast spin echo Cartesian applications). Some trajectories and/or sequences may also be more sensitive to errors from trajectory deviations which would preclude the use of repeated center of k-space measures of data inconsistency. In these cases, weights must be derived from signal modeling, measured from a pre-scan consisting of repeated samples of the same line in k-space, or measured using FID navigators.

Acknowledgments

We acknowledge GE Healthcare and NIH Grants R01NS065034, R01NS066982, RC1 EB010384-01, and R01HL072260-05 for their assistance and support.

Appendix: 2D Bitreverse Algorithm

The 2D bitreverse algorithm is an extension of more commonly utilized 1D methods and for N by M is performed as follows (written for Matlab):

```
function Order2D = bitreverse2D(M,N)
OrderM= bitreverse1D(M);
OrderN= bitreverse1D(N);
[i,j] = meshgrid(0:M-1,0:N-1);
Order2D= N*OrderM(1+mod(i+j,M)) + OrderN(j+1);
```

```
function Order1D = bitreverse1D(N)
Bits= ceil(log2(N));
Rn= bitrevorder(0:2^Bits-1);
Rn= Rn(1:N);
OrderN=sortrows([ (0:N-1)' Rx'],2);
OrderN(:,2)=0:N-1;
OrderN=sortrows(OrderN,1);
Order1D = OrderX(:,2);
```

References

1. Sodickson DK, Manning WJ. Simultaneous acquisition of spatial harmonics (SMASH): fast imaging with radiofrequency coil arrays. Magn Reson Med. 1997; 38(4):591–603. [PubMed: 9324327]
2. Pruessmann KP, Weiger M, Scheidegger MB, Boesiger P. SENSE: sensitivity encoding for fast MRI. Magn Reson Med. 1999; 42(5):952–962. [PubMed: 10542355]
3. Lustig M, Donoho D, Pauly JM. Sparse MRI: The application of compressed sensing for rapid MR imaging. Magn Reson Med. 2007; 58(6):1182–1195. [PubMed: 17969013]
4. Block KT, Uecker M, Frahm J. Undersampled radial MRI with multiple coils. Iterative image reconstruction using a total variation constraint. Magn Reson Med. 2007; 57(6):1086–1098. [PubMed: 17534903]
5. Noll DC, Nishimura DG, Macovski A. Homodyne Detection in Magnetic-Resonance-Imaging. Ieee Transactions on Medical Imaging. 1991; 10(2):154–163. [PubMed: 18222812]
6. Hu HH, Haider CR, Campeau NG, Huston J 3rd, Riederer SJ. Intracranial contrast-enhanced magnetic resonance venography with 6.4-fold sensitivity encoding at 1.5 and 3.0 Tesla. J Magn Reson Imaging. 2008; 27(3):653–658. [PubMed: 18224674]
7. Hennig J, Friedburg H. Clinical applications and methodological developments of the RARE technique. Magn Reson Imaging. 1988; 6(4):391–395. [PubMed: 3185132]

8. Hennig J, Weigel M, Scheffler K. Multiecho sequences with variable refocusing flip angles: optimization of signal behavior using smooth transitions between pseudo steady states (TRAPS). Magn Reson Med. 2003; 49(3):527–535. [PubMed: 12594756]
9. Busse RF, Hariharan H, Vu A, Brittain J. Fast spin echo sequences with very long echo trains: Design of variable refocusing flip angle schedules and generation of clinical contrast. Magn Reson Med. 2006; 55(5):1030–1037. [PubMed: 16598719]
10. Oshio K, Feinberg DA. GRASE (Gradient- and spin-echo) imaging: a novel fast MRI technique. Magn Reson Med. 1991; 20(2):344–349. [PubMed: 1775061]
11. Noll DC, Meyer CH, Pauly JM, Nishimura DG, Macovski A. A Homogeneity Correction Method for Magnetic-Resonance-Imaging with Time-Varying Gradients. Ieee Transactions on Medical Imaging. 1991; 10(4):629–637. [PubMed: 18222870]
12. Noll DC, Pauly JM, Meyer CH, Nishimura DG, Macovski A. Deblurring for non-2D Fourier transform magnetic resonance imaging. Magnetic Resonance in Medicine. 1992; 25(2):319–333. [PubMed: 1614315]
13. Markl M, Bammer R, Alley MT, Elkins CJ, Draney MT, Barnett A, Moseley ME, Glover GH, Pelc NJ. Generalized reconstruction of phase contrast MRI: analysis and correction of the effect of gradient field distortions. Magn Reson Med. 2003; 50(4):791–801. [PubMed: 14523966]
14. Hoge WS, Tan H, Kraft RA. Robust EPI Nyquist ghost elimination via spatial and temporal encoding. Magn Reson Med. 2010; 64(6):1781–1791. [PubMed: 20665898]
15. Pruessmann KP, Weiger M, Bornert P, Boesiger P. Advances in sensitivity encoding with arbitrary k-space trajectories. Magn Reson Med. 2001; 46(4):638–651. [PubMed: 11590639]
16. Griswold MA, Jakob PM, Heidemann RM, Nittka M, Jellus V, Wang J, Kiefer B, Haase A. Generalized autocalibrating partially parallel acquisitions (GRAPPA). Magn Reson Med. 2002; 47(6):1202–1210. [PubMed: 12111967]
17. Sutton BP, Noll DC, Fessler JA. Fast, iterative image reconstruction for MRI in the presence of field inhomogeneities. IEEE Trans Med Imaging. 2003; 22(2):178–188. [PubMed: 12715994]
18. Block KT, Uecker M, Frahm J. Model-based iterative reconstruction for radial fast spin-echo MRI. IEEE Trans Med Imaging. 2009; 28(11):1759–1769. [PubMed: 19502124]
19. Grabe M. Estimation of measurement uncertainties - an alternative to the ISO Guide. Metrologia. 2001; 38(2):97–106.
20. Brau AC, Brittain JH. Generalized self-navigated motion detection technique: Preliminary investigation in abdominal imaging. Magn Reson Med. 2006; 55(2):263–270. [PubMed: 16408272]
21. Lu A, Brodsky E, Grist TM, Block W. Rapid Fat-Suppressed Isotropic Steady-State Free Precession Using True 3D Multiple-Half-Echo Projection Reconstruction. Magn Reson Med. 2005; 53:692–699. [PubMed: 15723411]
22. Gmitro AF, Kono M, Theilmann RJ, Altbach MI, Li Z, Trouard TP. Radial GRASE: implementation and applications. Magn Reson Med. 2005; 53(6):1363–1371. [PubMed: 15906298]
23. Aubert-Broche B, Evans AC, Collins L. A new improved version of the realistic digital brain phantom. Neuroimage. 2006; 32(1):138–145. [PubMed: 16750398]
24. Song HK, Dougherty L. k-space weighted image contrast (KWIC) for contrast manipulation in projection reconstruction MRI. Magn Reson Med. 2000; 44(6):825–832. [PubMed: 11108618]
25. Theilmann RJ, Gmitro AF, Altbach MI, Trouard TP. View-ordering in radial fast spin-echo imaging. Magn Reson Med. 2004; 51(4):768–774. [PubMed: 15065250]
26. Wilson DW, Tsui BMW. Spatial resolution properties of FB and ML-EM reconstruction methods. Oct 31.Nov 31.1993 :1189–1193.
27. McKenzie CA, Yeh EN, Ohliger MA, Price MD, Sodickson DK. Self-calibrating parallel imaging with automatic coil sensitivity extraction. Magn Reson Med. 2002; 47(3):529–538. [PubMed: 11870840]
28. Larson AC, White RD, Laub G, McVeigh ER, Li D, Simonetti OP. Self-gated cardiac cine MRI. Magn Reson Med. 2004; 51(1):93–102. [PubMed: 14705049]

29. Samsonov AA, Velikina J, Jung Y, Kholmovski EG, Johnson CR, Block WF. POCS-enhanced correction of motion artifacts in parallel MRI. Magn Reson Med. 2010; 63(4):1104–1110. [PubMed: 20373413]

30. van Vaals JJ, Brummer ME, Dixon WT, Tuithof HH, Engels H, Nelson RC, Gerety BM, Chezmar JL, den Boer JA. “Keyhole” method for accelerating imaging of contrast agent uptake. Journal of Magnetic Resonance Imaging. 1993; 3(4):671–675. [PubMed: 8347963]

31. Liu J, Redmond MJ, Brodsky EK, Alexander AL, Lu A, Thornton FJ, Schulte MJ, Grist TM, Pipe JG, Block WF. Generation and visualization of four-dimensional MR angiography data using an undersampled 3-D projection trajectory. IEEE Trans Med Imaging. 2006; 25(2):148–157. [PubMed: 16468449]

32. Osborn, MR. Finite Algorithms in Optimization and Data Analysis. New York, NY, USA: John Wiley & Sons, Inc; 1985.

33. Huber, PJ. Robust statistics. Vol. ix. New York: Wiley; 1981. p. 308

34. Bydder, GM. The use of robust methods to reduce image artifacts. Toronto, Canada: 2003. p. 482

35. Busse RF, Brau AC, Vu A, Michelich CR, Bayram E, Kijowski R, Reeder SB, Rowley HA. Effects of refocusing flip angle modulation and view ordering in 3D fast spin echo. Magn Reson Med. 2008; 60(3):640–649. [PubMed: 18727082]

36. Lustig M, Pauly JM. SPIRiT: Iterative self-consistent parallel imaging reconstruction from arbitrary k-space. Magn Reson Med. 2010; 64(2):457–471. [PubMed: 20665790]

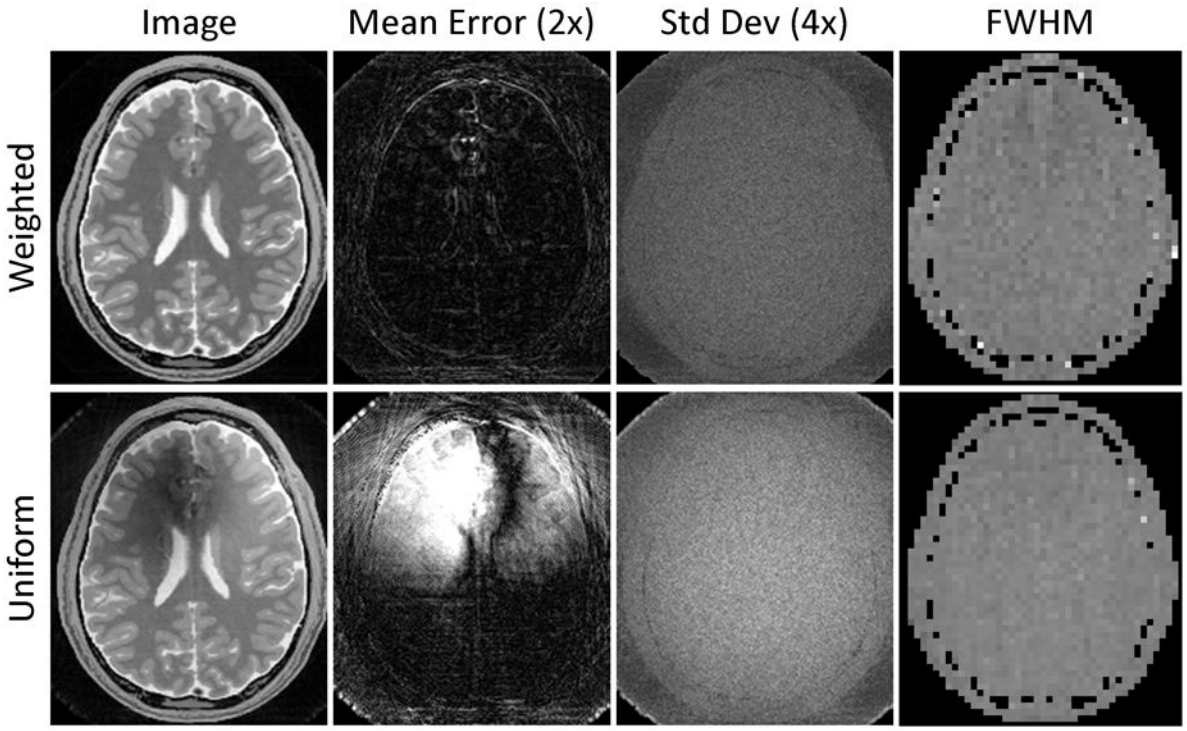

Figure 1.
2D digital phantom images from a single realization, mean error images window leveled 2x, noise images window leveled 4x, and FWHM images window leveled from 0.5 to 1.5 of the nominal resolution. Using uniform data weighting results in TE bias, artifacts in and around areas of off-resonance precession, and increased streak artifacts. RMSE error over the entire phantom is reduced from 9.6% to 2.3% utilizing weighting. Noise is also reduced from 1.6% to 1.1% in the weighted image. The average FWHM was 0.9941 using weighting and 1.0074 without.

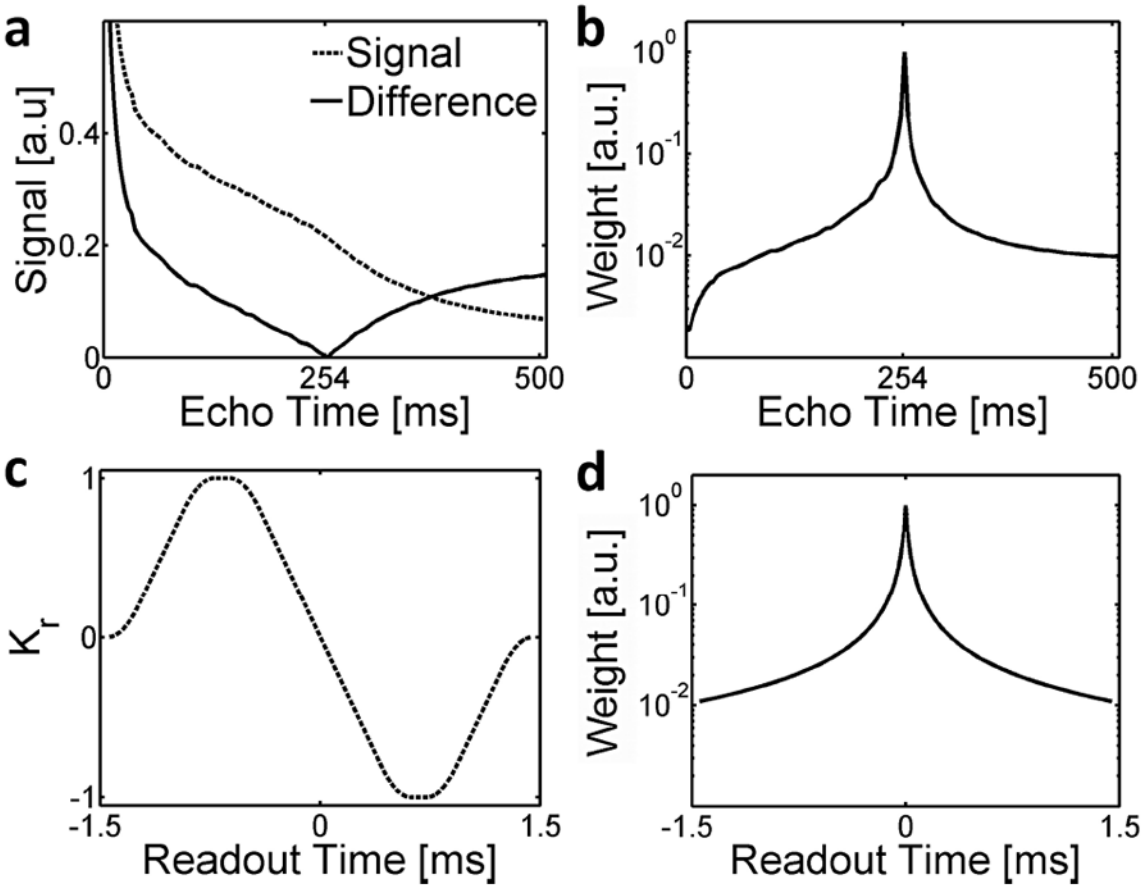

Figure 2.

Weighting functions derived for a volunteer. Measured signal magnitude from the center of k-space and difference with respect to the central (64th) echo (a). The corresponding weighting function along the spin echo dimension is shown in (b). The k-space radius along a given readout (c) show shows the 4 half lines collected in k-space hitting the center of k-space 3 times within a given readout window. Weighting in the readout dimension (d) is determined using the center of the readout as a reference and assumed modeling of fat/water and B0 heterogeneity.

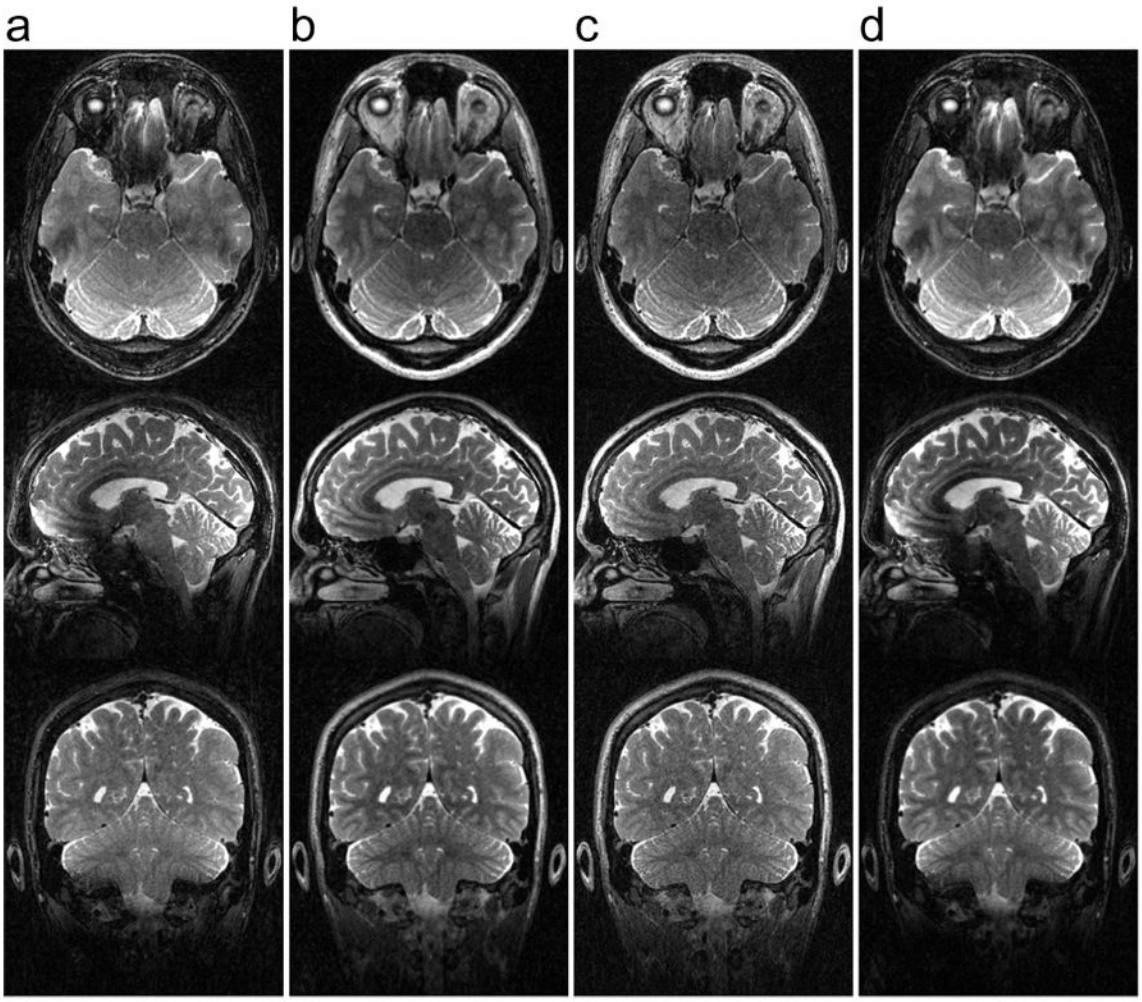

Figure 3.
Axial, sagittal, and coronal reformats of the same 3D radial data reconstructed with uniform weighting (a), data consistency weighting in both the readout and echo train dimension (b), weighting only in the readout direction (c), and weighting only in the echo train dimension (d). Echo train weighting improves contrast (b/d) and readout weighting reduces artifacts in areas of off resonance (b/d) compared to uniform weighting.

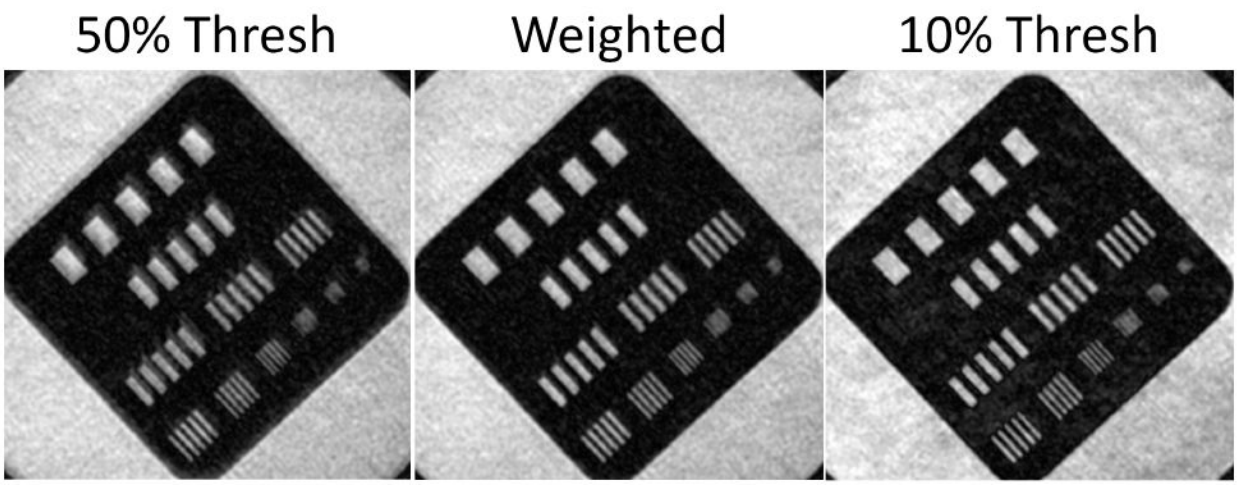

Figure 4.
Images on the moving phantom using 50 and 20% thresholds and the data consistency weighting approach. Images with the weighted approach have minimal motion blur while avoiding substantial artifacts from undersampling.

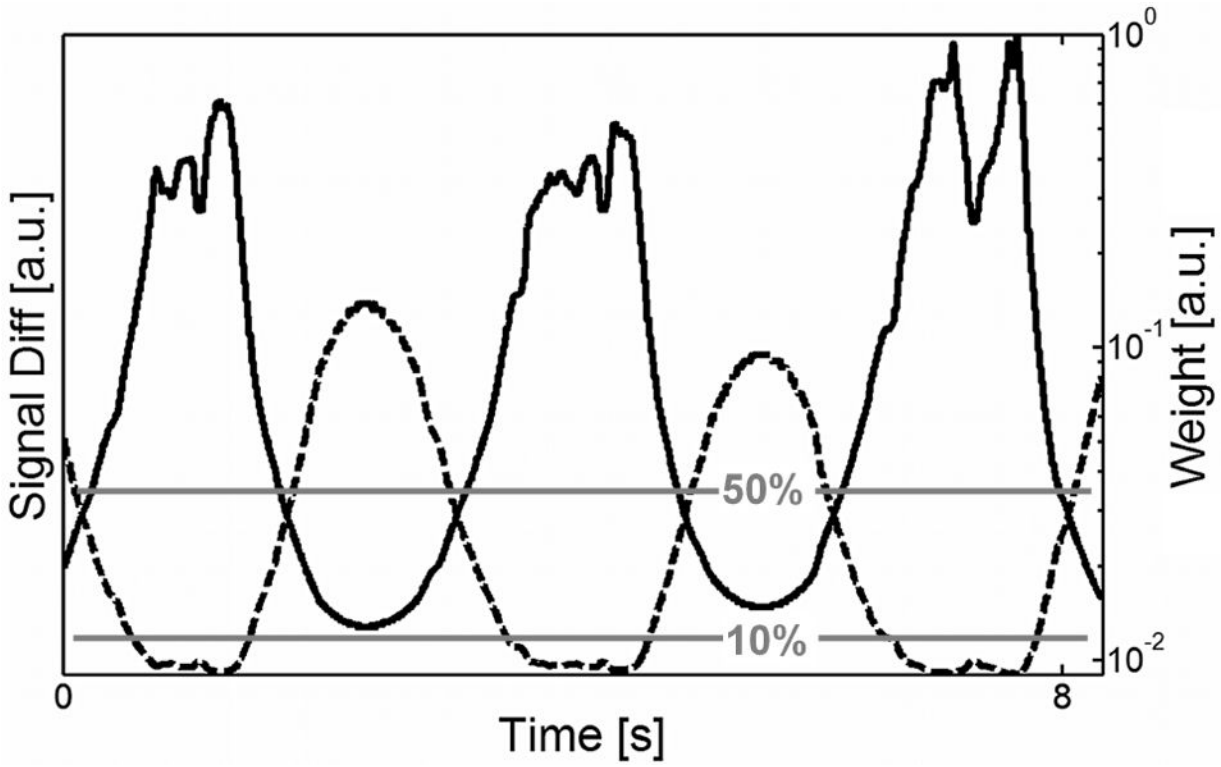

Figure 5.
Signal differences (dashed line) derived in vivo. Simple 10 and 50% thresholds are shown with all projections below that line utilized for reconstruction. The weighting function (solid line) down weights areas of high signal difference.

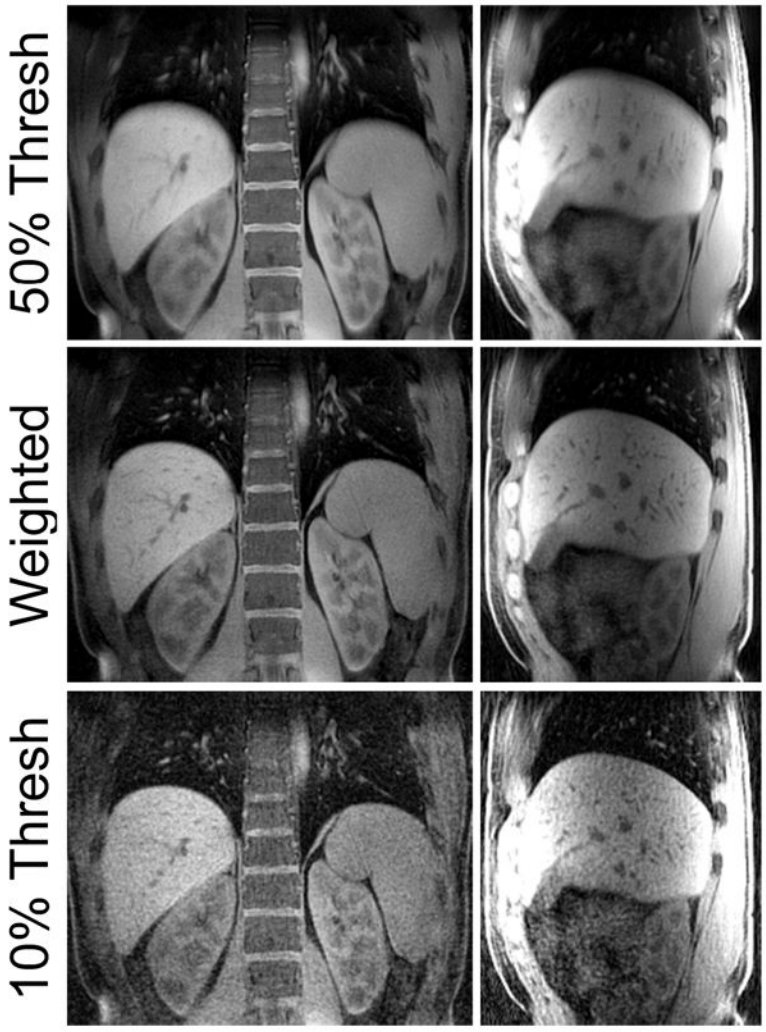

Figure 6.
Coronal and sagittal reformats of utilizing the schemes shown in Figure 5. Thresholding with a 50% threshold produces images with high SNR but with substantial blurring. In contrast, 10% thresholding produces images with minimal blur, but they are noisy. With setting acceptance windows at all the weighted approach produces images with high SNR and minimal motion blur.